Author's accepted manuscript

A 3D Non-Stationary Cluster Channel Model for Human Activity Recognition

Ahmed Abdelgawwad and Matthias Pätzold

Department of Information and Communication Technology

Faculty of Engineering and Science, University of Agder

P.O. Box 509, NO-4898 Grimstad, Norway

E-mails: {ahmed.abdel-gawwad, matthias.paetzold}@uia.no

Abstract — **This paper proposes a three-dimensional (3D) non-stationary fixed-to-fixed indoor channel simulator model for human activity recognition. The channel model enables the formulation of temporal variations of the received signal caused by a moving human. The moving human is modelled by a cluster of synchronized moving scatterers. Each of the moving scatterers in a cluster is described by a 3D deterministic trajectory model representing the motion of specific body parts of a person, such as wrists, ankles, head, and waist. We derive the time-variant (TV) Doppler frequencies caused by the motion of each moving scatterer by using the TV angles of motion, angles of arrival, angles of departure. Moreover, we derive the complex channel gain of the received signal. Furthermore, we analyze the TV Doppler power spectral density of the complex channel gain by using the concept of the spectrogram and present its expression in approximated form. Also, we derive the TV mean Doppler shift and TV Doppler spread from the approximated spectrogram. The accuracy of the results is validated by simulations. The channel simulator is beneficial for the development of activity recognition systems with non-wearable devices as the demand for such systems has increased recently.**

C.1   Introduction

In 2017, according to the United Nations' World Aging Report the number of people age 60 and older was 962 million, which is more than double the 1980 figure [1]. By 2050, the number of over-60s is expected to double from 2017. Also, the number of people age 80 and older is expected to triple from 137 million to 425 million between 2017 and 2050. These figures indicate a high demand for eldercare systems, such as in-home activity recognition systems to classify normal activities such as walking and sitting as well as abnormal activities such as falls.

In the literature, fall detection systems have been developed using wearable inertial measurement units (IMUs) [2] and video surveillance systems [3]. The main drawback of such systems is that the user may forget to wear the sensor or might go outside the coverage area of the video surveillance system. Another disadvantage is that these systems break the privacy of the user. To overcome these drawbacks, radio-frequency-based (RF-based) non-wearable human tracking systems have been introduced by the authors of [4]. Such systems use RF-based sensors that operate by using frequency-modulated carrier waves. These systems track humans by using wave components scattered by their bodies.

The compound Doppler effect caused by moving scatterers has been studied in two-dimensional fixed-to-mobile channels in [3]. The time-variant (TV) Doppler effect caused by moving scatterers has been modelled in F2F non-stationary indoor channels [5,6], and in 3D non-stationary MIMO channels in [7]. In order to analyze the TV Doppler power spectrum, we use the concept of the spectrogram, which is one of the time-frequency distributions that provides insight into the TV power spectral density of multicomponent signals [8]. It is also used in applications such as fall detection [9,10], classification of human activities [11], and enables to distinguish between armed and unarmed persons for security and rescue services [12]. The main drawback of the spectrogram is the cross-term that has an impact on its resolution. Contributions have been introduced to overcome this problem in mobile fading channels in [13].

The goal of this paper is to model the influence of different body parts of a walking person on the Doppler power spectrum characteristics of three-dimensional (3D) fixed-to-fixed (F2F) indoor channels. We introduce a 3D non-stationary F2F channel model with fixed scatterers and clusters of synchronized moving scatterers as an extension to the model presented in [6]. An expression of the TV Doppler frequency of each moving scatterer in a cluster is provided in terms of the TV speed, the TV azimuth angles of departure (AAOD), the TV elevation angles of departure (EAOD), the TV azimuth angles of arrival (AAOA), the TV elevation angles of arrival (EAOA), the TV horizontal angles of motion (HAOM), and the TV vertical angles of motion (VAOM). Furthermore, the instantaneous channel phases and the complex channel gain of the 3D non-stationary F2F multipath fading channel are presented. Moreover, an approximation of the spectrogram of the complex channel gain is provided as a sum of

the auto-term and the cross-term. The auto-term gives us an approximation of the true TV Doppler power spectral density of the complex channel gain, while the cross-term is considered as an undesired spectral interference term that reduces the resolution of the spectrogram. The TV mean Doppler shift and the TV Doppler spread are also derived from the spectrogram. The novelty of this paper lies not only in presenting a non-stationary F2F model with fixed scatterers and clusters of moving scatterers, but also in presenting deterministic trajectory models of different body parts of a walking person.

The remaining sections of this paper are divided as follows. Section C.2 discusses a multipath propagation scenario with a fixed transmitter, a fixed receiver, fixed scatterers, and clusters of moving scatterers. Section C.3 derives an exact and approximate solution of the TV Doppler frequencies of the moving scatterers of the clusters, TV channel phases, complex channel gain, TV mean Doppler shift, and TV Doppler spread. Section C.4 presents an approximate solution of the spectrogram. By using the spectrogram, we compute the TV mean Doppler shift and the TV Doppler spread. Section C.5 discusses the numerical results, introduces realistic mathematical trajectory models of the motion of the major body parts of a walking human, and shows the influence of them on the spectrogram, the TV mean Doppler shift, and the TV Doppler spread. Section C.6 summarizes our work and suggests possible ideas for future work.

C.2   The 3D Indoor Propagation Scenario

Consider the multipath propagation scenario in Fig. C.1. This scenario consists of a fixed transmitter (T_x), a fixed receiver (R_x), moving persons, and fixed objects. The transmitter and the receiver are located at (x^T, y^T, z^T) and (x^R, y^R, z^R), respectively. Each moving person is modelled by a cluster of synchronized moving scatterers $S_{n,m}^{\mathrm{M}}$ for $n = 1, 2, \ldots, N_m$ and $m = 1, 2, \ldots, N_c$, where N_m is the number of moving scatterers of the mth cluster, and N_c is the number of clusters. Each moving scatterer $S_{n,m}^{\mathrm{M}}$ has a starting position at $\left(x_{n,m}^{\mathrm{M}}, y_{n,m}^{\mathrm{M}}, z_{n,m}^{\mathrm{M}} \right)$. The 3D trajectory of the nth moving scatterer of the mth cluster is described by its TV speed $\mathrm{v}_{n,m}(t)$, TV HAOM $\alpha_{v_{n,m}}(t)$, and TV VAOM $\beta_{v_{n,m}}(t)$. In Fig. C.1, we have stationary objects, such as walls and furniture which are simply modelled as M fixed scatterers S_m^{F} for $m = 1, 2, \ldots, M$. Single bounce scattering and non-line-of-sight (NLOS) conditions are assumed. Moreover, it is assumed that the T_x and R_x are deployed with omnidirectional antennas.

C.3   The Complex Channel Gain

The TV Doppler frequency $f_{n,m}(t)$ caused by the TV speed $\mathrm{v}_{n,m}(t)$, TV HAOM $\alpha_{v_{n,m}}(t)$, TV VAOM $\beta_{v_{n,m}}(t)$, TV AAOD $\alpha_{n,m}^T(t)$, TV EAOD $\beta_{n,m}^T(t)$, TV AAOA $\alpha_{n,m}^R(t)$, and TV EAOA
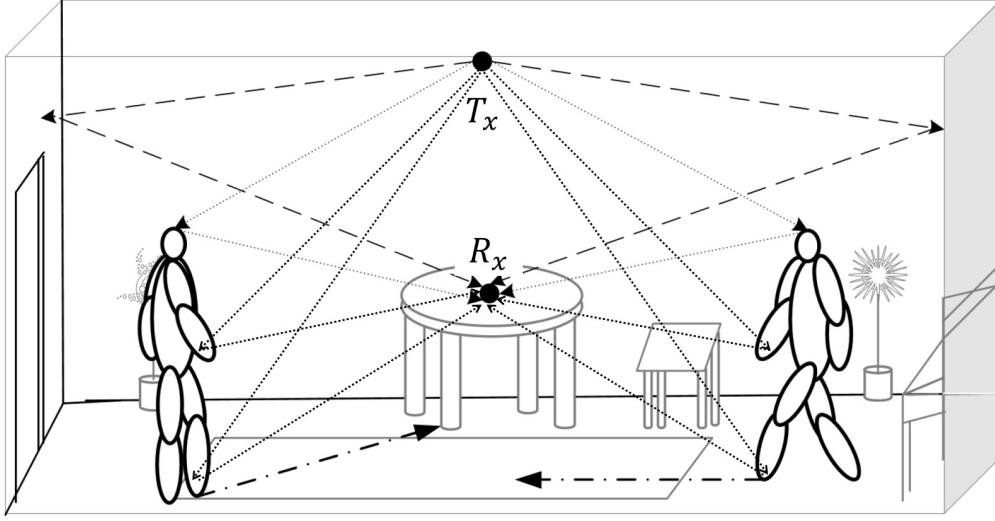
Figure C.1: A 3D non-stationary multipath propagation scenario with moving persons, a fixed transmitter, a fixed receiver, and fixed objects.

$\beta_{n,m}^R(t)$ of the nth moving scatterer $S_{n,m}^{\mathrm{M}}$ of the mth cluster is given by [6]

$$
\begin{aligned}
f_{n,m}(t) = -f_{n,m,\mathrm{max}}(t) \bigg\{ &\cos\left(\beta_{v_{n,m}}(t)\right) \\
\times \big[&\cos\left(\beta_{n,m}^T(t)\right)\cos\left(\alpha_{n,m}^T(t) - \alpha_{v_{n,m}}(t)\right) \\
+ &\cos\left(\beta_{n,m}^R(t)\right)\cos\left(\alpha_{v_{n,m}}(t) - \alpha_{n,m}^R(t)\right) \big] \\
+ &\sin\left(\beta_{v_{n,m}}(t)\right)\big[\sin\left(\beta_{n,m}^T(t)\right) + \sin\left(\beta_{n,m}^R(t)\right)\big] \bigg\}
\end{aligned}
\tag{C.1}
$$

where

$$
f_{n,m,\mathrm{max}}(t) = \frac{\mathrm{v}_{n,m}(t)\, f_0}{c}.
\tag{C.2}
$$

The parameters f_0 and c in (C.2) denote the carrier frequency of the transmitted signal and the speed of light, respectively. The expression in (C.2) represents the maximum Doppler shift caused by the motion speed of the nth moving scatterer $S_{n,m}^{\mathrm{M}}$ of the mth cluster. The expressions of the TV HAOM $\alpha_{v_{n,m}}(t)$, TV VAOM $\beta_{v_{n,m}}(t)$, TV AAOD $\alpha_{n,m}^T(t)$, TV EAOD $\beta_{n,m}^T(t)$, TV AAOA $\alpha_{n,m}^R(t)$, and TV EAOA $\beta_{n,m}^R(t)$ can be found in [6]. The expression of the Doppler frequency $f_{n,m}(t)$ in (C.1) can be approximated by using L piecewise linear functions of time as

$$
f_{n,m}(t) \approx f_{n,m,l}(t) = f_{n,m}(t_l) + k_{n,m,l}(t - t_l)
\tag{C.3}
$$

for $t_l < t \leq t_{l+1}$ and $l = 0, 1, \ldots, L$, where

$$
k_{n,m,l} = \frac{f_{n,m}(t_{l+1}) - f_{n,m}(t_l)}{t_{l+1} - t_l}.
\tag{C.4}
$$

Note that the interval length between two time instances in a row, i.e., $\Delta_l = t_{l+1} - t_l$, is the same for all values of $l = 0, 1, \ldots, L - 1$, where L is the number of the time instances at which the Doppler frequencies were approximated. The parameter $k_{n,m,l}$ in (C.4) expresses the rate of change of the Doppler frequency $f_{n,m}(t)$ at time $t = t_l$.

The instantaneous channel phase $\theta_{n,m,\mathrm{M}}(t)$ caused by the motion of the nth moving scatterer of the mth cluster is given by [14]

$$\theta_{n,m,\mathrm{M}}(t) = 2\pi \int_{-\infty}^{t} f_{n,m}(t')dt' = \theta_{n,m,\mathrm{M}} + 2\pi \int_{0}^{t} f_{n,m}(t')dt'. \tag{C.5}$$

The first term in (C.5) is the initial phase shift, which is modelled as a zero-mean random variable with a uniform distribution between $-\pi$ and π. Hence, the instantaneous channel phase $\theta_{n,m,\mathrm{M}}(t)$ in (C.5) is a stochastic process. After obtaining the instantaneous channel phase $\theta_{n,m,\mathrm{M}}(t)$, the complex channel gain $\mu(t)$ consisting of $\sum_{m=1}^{N_\mathrm{C}} N_m + M$ received multipath components is modelled by

$$\mu(t) = \sum_{m=1}^{N_\mathrm{C}} \sum_{n=1}^{N_m} c_{n,m,\mathrm{M}} \, e^{j\theta_{n,m,\mathrm{M}}(t)} + \sum_{m=1}^{M} c_{m,\mathrm{F}} \, e^{j\theta_{m,\mathrm{F}}}. \tag{C.6}$$

The double sum in the first term in (C.6) represents the sum of the multipath components corresponding to N_C clusters and the N_m moving scatterers therein. Each moving scatterer in a cluster has a stochastic channel phase $\theta_{n,m,\mathrm{M}}(t)$, and a constant path gain $c_{n,m,\mathrm{M}}$. The second term in (C.6) designates the sum of the multipath components associated with the M fixed scatterers with constant path gains $c_{m,\mathrm{F}}$ and random phases $\theta_{m,\mathrm{F}}$. It should be noted that the phases $\theta_{n,m,\mathrm{M}}$ and $\theta_{m,\mathrm{F}}$ are modelled as zero-mean random variables with a uniform distribution that ranges from $-\pi$ to π. The complex channel gain $\mu(t)$ in (C.6) is a stochastic model for a 3D non-stationary indoor channel with clusters of moving scatterers, fixed scatterers, fixed transmitter, and fixed receiver. The TV mean Doppler shift and the TV Doppler spread of this model can be expressed as [14]

$$B_f^{(1)}(t) = \frac{\sum\limits_{m=1}^{N_\mathrm{C}} \sum\limits_{n=1}^{N_m} c_{n,m,\mathrm{M}}^2 \, f_{n,m}(t)}{\sum\limits_{m=1}^{N_\mathrm{C}} \sum\limits_{n=1}^{N_m} c_{n,m,\mathrm{M}}^2 + \sum\limits_{m=1}^{M} c_{m,\mathrm{F}}^2} \tag{C.7}$$

and

$$B_f^{(2)}(t) = \sqrt{\frac{\sum\limits_{m=1}^{N_\mathrm{C}} \sum\limits_{n=1}^{N_m} c_{n,m,\mathrm{M}}^2 \, f_{n,m}^2(t)}{\sum\limits_{m=1}^{N_\mathrm{C}} \sum\limits_{n=1}^{N_m} c_{n,m,\mathrm{M}}^2 + \sum\limits_{m=1}^{M} c_{m,\mathrm{F}}^2} - \left(B_f^{(1)}(t)\right)^2} \tag{C.8}$$

respectively.

C.4 Spectrogram Analysis

The spectrogram $S_\mu(f,t)$ of the complex channel gain $\mu(t)$ is computed in three steps. *Step 1*: we multiply the complex channel gain $\mu(t)$ by a sliding window to obtain the short-time signal. In this paper, we use the Gaussian window function

$$h(t) = \frac{1}{\sqrt{\sigma_w\sqrt{\pi}}}e^{-\frac{t^2}{2\sigma_w^2}} \tag{C.9}$$

where σ_w denotes the window spread parameter. The window function is real and even and has a normalized energy of $\int_{-\infty}^{\infty} h^2(t)dt = 1$. The short-time complex channel gain is given according to [15, Eq. (2.3.1)] by

$$x(t',t) = \mu(t')h(t'-t) \tag{C.10}$$

where the variables t' and t are the running time and the observation time, respectively. Continuing with *Step 2*, we calculate the short-time-Fourier-transform (STFT) by computing the Fourier-transform of the short-time signal $X(t',t)$ w.r.t. the running time t' as follows

$$X(f,t) = \int_{-\infty}^{\infty} x(t',t)e^{-j2\pi ft'}dt'. \tag{C.11}$$

For the sake of brevity, we do not provide the expression for the STFT. Finally, the last step is multiplying the STFT $X(f,t)$ in (C.11) by its complex conjugate to obtain the spectrogram $S_\mu(f,t)$ as

$$S_\mu(f,t) = |X(f,t)|^2 = S_\mu^{(a)}(f,t) + S_\mu^{(c)}(f,t) \tag{C.12}$$

where the functions $S_\mu^{(a)}(f,t)$ and $S_\mu^{(c)}(f,t)$ denote the auto-term and the cross-term, respectively. By using the approximate expression of the Doppler frequency $f_{n,m,l}(t)$ in (C.3), the approximate solution of the auto-term $S_\mu^{(a)}(f,t)$ is given by

$$S_\mu^{(a)}(f,t) = \sum_{m=1}^{N_{\mathrm{C}}} \sum_{n=1}^{N_m} c_{n,m,\mathrm{M}}^2 \, G\left(f, f_{n,m,l}(t), \sigma_{n,m,l,\mathrm{M}}^2\right)$$

$$+ \sum_{m=1}^{M} c_{m,\mathrm{F}}^2 \, G\left(f, 0, \sigma_{m,\mathrm{F}}^2\right) \tag{C.13}$$

for $t_l < t \le t_{l+1}$ $(l = 0, 1, \cdots, L-1)$, where

$$G(x, \mu, \sigma^2) = \frac{e^{\frac{-(x-\mu)^2}{2\sigma^2}}}{\sqrt{2\pi\sigma^2}} \tag{C.14}$$

$$\sigma_{n,m,l,\mathrm{M}}^2 = \frac{1 + (2\pi\sigma_w^2 k_{n,m,l})^2}{2(2\pi\sigma_w)^2} \tag{C.15}$$

$$\sigma_{m,\mathrm{F}}^2 = \frac{1}{2(2\pi\sigma_w)^2}. \tag{C.16}$$

The auto-term $S_\mu^{(a)}(f,t)$ given by (C.13) consists of a sum of $\sum_{m=1}^{N_\mathrm{C}} N_m + M$ components. It is a real and positive function that represents an approximation of the desired TV Doppler power spectral density of the complex channel gain $\mu(t)$ discussed in Section C.3. The first term of the auto-term $S_\mu^{(a)}(f,t)$ in (C.13) is a double sum of weighted Gaussian functions, where each component of this term corresponds to the nth moving scatterer of the mth cluster. Note that the Gaussian functions of the first term of the auto-term $S_\mu^{(a)}(f,t)$ are weighted by the squared path gain $c_{n,m,\mathrm{M}}^2$ and centered on the approximated Doppler frequency $f_{n,m,l}(t)$ of the nth moving scatterer of the mth cluster. The second term of the auto-term $S_\mu^{(a)}(f,t)$ in (C.13) is also a sum of Gaussian functions factorized by the squared path gain $c_{m,\mathrm{F}}^2$ of each fixed scatterer and centered on the zero-frequency value as a fixed scatterer does not introduce a Doppler shift in F2F channels. The parameters in (C.15) and (C.16) denote the variances of the Gaussian functions presented in (C.13). It should be mentioned that the variance of the Gaussian function in the first term of the auto-term in (C.13) is dependent on the slope of the Doppler frequency $f_{n,m,l}(t)$ given by (C.4). It should also be noted that the auto-term in (C.13) does not depend on the random channel phases $\theta_{n,m,\mathrm{M}}$ and $\theta_{n,\mathrm{F}}$.

The cross-term $S_\mu^{(c)}(f,t)$ is presented in (C.19) at the top of the next page. It represents an undesired spectral interference term that reduces the resolution of the spectrogram. The cross-term $S_\mu^{(c)}(f,t)$ in (C.19) has $(\sum_{m=1}^{N_\mathrm{C}} N_m + M)(\sum_{m=1}^{N_\mathrm{C}} N_m + M - 1)/2$ components. It is a real function and can have positive or negative values. Unlike the auto-term $S_\mu^{(a)}(f,t)$, the cross-term $S_\mu^{(c)}(f,t)$ depends on the random channel phases $\theta_{n,m,\mathrm{M}}$ and $\theta_{n,\mathrm{F}}$. Thus, it can be removed by taking the average of the spectrogram $S_\mu(f,t)$ over the phases, i.e., $E\{S_\mu(f,t)\}\,|_{\theta_{n,m,\mathrm{M}},\theta_{m,\mathrm{F}}} = S_\mu^{(a)}(f,t)$. The parameter $\mu_{m,\mathrm{F}}$ (function $\mu_{n,k,\mathrm{M}}(t)$) in (C.19) denotes the complex channel gain of the mth fixed scatterer (nth moving scatterer of the kth cluster). The operators $\Re\{\cdot\}$ and $\{*\}$ in (C.19) compute the real part and the complex conjugate of a complex function, respectively. The parameters $\sigma_{x,n,m,l,\mathrm{M}}^2$ and $\sigma_{x,m,\mathrm{F}}^2$ in (C.19) are given by

$$\sigma_{x,n,m,l,\mathrm{M}}^2 = \frac{1 - j2\pi\sigma_w^2 k_{n,m,l}}{(2\pi\sigma_w)^2} \tag{C.17}$$

$$\sigma_{x,m,\mathrm{F}}^2 = \frac{1}{(2\pi\sigma_w)^2} \tag{C.18}$$

respectively. The TV mean Doppler shift $B_\mu^{(1)}(t)$ and the TV Doppler spread $B_\mu^{(2)}(t)$ can be obtained by using the spectrogram as follows [5]

$$B_\mu^{(1)}(t) = \frac{\int\limits_{-\infty}^{\infty} f S_\mu(f,t)\,df}{\int\limits_{-\infty}^{\infty} S_\mu(f,t)\,df} \tag{C.20}$$

$$S_\mu^{(c)}(f,t) = \frac{2}{\sigma_w \sqrt{\pi}} \Re \Bigg\{ \sum_{m=1}^{N_C} \sum_{n=1}^{N_m-1} \sum_{k=n+1}^{N_m} G\left(f, f_{n,m,l}(t), \sigma_{x,n,m,l,M}^2\right)$$

$$\times\, G^*\left(f, f_{k,m,l}(t), \sigma_{x,k,m,l,M}^2\right) \mu_{n,m,M}(t)\, \mu_{k,m,M}^*(t)$$

$$+ \sum_{n=1}^{M-1} \sum_{m=n+1}^{M} G(f, 0, \sigma_{x,n,F}^2) G^*(f, 0, \sigma_{x,m,F}^2)\, \mu_{n,F} \mu_{m,F}^*$$

$$+ \sum_{m=1}^{N_C} \sum_{n=1}^{N_m} \sum_{k=1}^{M} G\left(f, f_{n,m,l}(t), \sigma_{x,n,m,l,M}^2\right) G^*(f, 0, \sigma_{x,k,F}^2) \mu_{n,m,M}(t) \mu_{k,F}^*$$

$$+ \sum_{m=1}^{N_C-1} \sum_{q=k+1}^{N_C} \sum_{n=1}^{N_m} \sum_{k=1}^{N_q} G\left(f, f_{n,m,l}(t), \sigma_{x,n,m,l,M}^2\right) G^*\left(f, f_{k,q,l}(t), \sigma_{x,k,q,l,M}^2\right) \mu_{n,m,M}(t)\, \mu_{k,q,M}^*(t) \Bigg\}$$

$$\text{(C.19)}$$

and

$$B_\mu^{(2)}(t) = \sqrt{\frac{\int\limits_{-\infty}^{\infty} f^2 S_\mu(f,t) df}{\int\limits_{-\infty}^{\infty} S_\mu(f,t) df} - \left(B_\mu^{(1)}(t)\right)^2} \tag{C.21}$$

respectively.

C.5   Numerical Results

In this section, we discuss some numerical results regarding the spectrogram, the TV mean Doppler shift, and the TV Doppler spread.

First, we introduce the trajectory models for the ankles, wrists, trunk (waist), and head of a walking person. The velocities of the right ankle and left ankle along with the x-axis are defined as piecewise functions by

$$v_{x,\mathrm{RA}}(t) = \begin{cases} v_x \left(1 - \cos\left(\frac{2\pi t}{T_{\mathrm{step}}}\right)\right), & \text{if } 0 \leq t \leq T_{\mathrm{step}}, \\ 0, & \text{if } T_{\mathrm{step}} < t \leq 2T_{\mathrm{step}} \end{cases} \tag{C.22}$$

$$v_{x,\mathrm{LA}}(t) = \begin{cases} 0, & \text{if } 0 \leq t \leq T_{\mathrm{step}} \\ v_x \left(1 - \cos\left(\frac{2\pi t}{T_{\mathrm{step}}}\right)\right), & \text{if } T_{\mathrm{step}} \leq t \leq 2T_{\mathrm{step}} \end{cases} \tag{C.23}$$

respectively, where the parameter v_x (T_{step}) stands for the constant speed (step duration). The trajectories of the right ankle and left ankle in the vertical direction, i.e., in the direction

of the z-axis are computed by

$$z_{\text{RA}}(t) = \begin{cases} H_{\text{foot}}\left(1 - \cos(\frac{2\pi t}{T_{\text{step}}})\right), & \text{if } 0 \leq t \leq T_{\text{step}}, \\ 0, & \text{if } T_{\text{step}} < t \leq 2T_{\text{step}} \end{cases} \tag{C.24}$$

$$z_{\text{LA}}(t) = \begin{cases} 0, & \text{if } 0 \leq t \leq T_{\text{step}}, \\ H_{\text{foot}}\left(1 - \cos(\frac{2\pi t}{T_{\text{step}}})\right), & \text{if } T_{\text{step}} < t \leq 2T_{\text{step}} \end{cases} \tag{C.25}$$

respectively, where the parameter H_{foot} represents the maximum displacement of the foot while walking along the z-axis. The ankle models presented in (C.22)–(C.25) were inspired by the ankle model of humanoid robotics provided in [16]. Next, we define the displacements of the right and left wrist in the x-direction as follows

$$x_{\text{RW}}(t) = \frac{v_x t}{2} + x_{\text{w}} \cos\left(\frac{\pi t}{T_{\text{step}}}\right) \tag{C.26}$$

$$x_{\text{LW}}(t) = \frac{v_x t}{2} - x_{\text{w}} \cos\left(\frac{\pi t}{T_{\text{step}}}\right) \tag{C.27}$$

respectively, where the parameter x_{w} denotes the maximum displacement of the wrists. The main reason for using a positive sign in (C.26) and a negative sign in (C.27) is that the displacement in the x-direction of the right (left) wrist is synchronous with the displacement of the left (right) ankle. Note that the period of the cosine functions in (C.26)–(C.27) is twice as long as in (C.22)–(C.23). The displacements in the z-direction of the right and left wrist are the same and calculated by

$$z_{\text{RW}}(t) = z_{\text{LW}}(t) = z_{\text{w}} \cos\left(\frac{2\pi t}{T_{\text{step}}}\right) \tag{C.28}$$

where the parameter z_{w} denotes the maximum vertical displacement of the wrists. It should be mentioned that the displacements of the wrists are out of phase in the x-direction and in phase in the z-direction. The displacements in the x-direction and the z-direction of the head and waist have the same expression, which are given by [17, 18]

$$x_{\text{Head}}(t) = x_{\text{Waist}}(t) = \frac{v_x t}{2}$$

$$z_{\text{Head}}(t) = z_{\text{Waist}}(t) = H_{\text{H,W}}\left(1 - \cos\left(\frac{2\pi t}{T_{\text{step}}}\right)\right) \tag{C.29}$$

respectively, where the parameter $H_{\text{H,W}}$ in (C.29) designates the maximum vertical displacement in the z-direction. When generating the scenario for the walking person, we chose the values of T_{step}, v_x, H_{foot}, x_{w}, z_{w}, and $H_{\text{H,W}}$ to be $1\,\text{s}$, $0.8\,\text{m/s}$, $0.1\,\text{m}$, $0.1\,\text{m}$, $0.025\,\text{m}$, and $0.025\,\text{m}$, respectively. The heights of ankles, wrists, head, and waist were set to $0.1\,\text{m}$, $1\,\text{m}$,

1.7 m, and 1.1 m, respectively. The number of walking steps were chosen to be 10 steps. Fig. C.2 depicts the displacements of the ankles, wrists, head, and waist in the x-direction. A good synchronization is shown in Fig. C.2 between the trajectories of the body parts, i.e., when the right ankle moves a step forward, the left wrist also swings forward, while the right wrist swings backward and the left leg stands on the ground. The forward displacements presented in Fig. C.2 in the x-direction of the ankles were computed by generating 5 piecewise functions of the forward velocities provided by (C.22) and (C.23) for the right ankle and left ankle, respectively. Then, the forward displacement is computed by integrating the forward velocities in (C.22) and (C.23) w.r.t. time t. Fig. C.3 shows a good synchronization between the displacements in the z-direction of the ankles, wrists, head, and waist, i.e., when the person takes a step forward with his right foot, the ankle moves upward in the z-direction until it crosses the left foot and then, it moves downward until it reaches the ground. The head and waist reach the maximum displacement at the time instant, in which the right or left foot reaches the maximum upward displacement. The wrists reach their maximum vertical displacements at the time instant, in which the heels are on the ground.

Fig C.4 depicts the walking scenario of the moving person in 3D. The number of clusters N_C was set to 1 and the number of moving scatterers in the cluster N_m was chosen to be 6. We used the same values of the motion parameters mentioned earlier in this section. The only difference is that the horizontal angle of motion $\alpha_{v_{n,m}}(t)$ was set to 15°, i.e., the direction of motion of the body was chosen to be 15°. The locations of the transmitter T_x and the receiver R_x were chosen to be (5.5 m, 2.5 m, 2.25 m) and (5 m, 2.5 m, 2.25 m), respectively. It is supposed that the LOS is blocked.

When computing the spectrogram, we chose the number of fixed scatterers M to be 6. Fig. C.5 depicts the result of the approximation of the spectrogram given by (C.12). The path gains of the moving scatterers and fixed scatterers are given by

$$c_{n,m,\mathrm{M}} = \sqrt{\frac{2\eta}{\sum_{m=1}^{N_C} N_m}} \qquad \text{and} \qquad c_{m,\mathrm{F}} = \sqrt{\frac{2(1-\eta)}{M}} \qquad \text{(C.30)}$$

respectively, where the parameter $\eta \leq 1$ is used for balancing the contribution of the fixed and moving scatterers on the mean power of the complex channel gain $\mu(t)$. Here, the parameter η was set to 0.6. We chose the value of 5.9 GHz for the carrier frequency f_0. The window spread parameter σ_w was set to 0.0335 s. Fig. C.5 shows the influence of the motion of major body parts on the spectrogram of $\mu(t)$. The spectrogram in Fig. C.5 is blurred due to the impact of the cross-term $S_\mu^{(c)}(f,t)$. The simulation results of the spectrogram are close to the analytical results, but they are not provided in the paper for brevity. In the simulation, we generated the values of the trajectories for the wrists, ankles, head, and waist in 3D using the mathematical models and their parameters provided earlier in this section. Then, we computed the HAOM $\alpha_{v_{n,m}}(t)$, VAOM $\beta_{v_{n,m}}(t)$, AAOA $\alpha_{n,m,\mathrm{M}}^{R}(t)$, EAOA $\beta_{n,m,\mathrm{M}}^{R}(t)$,
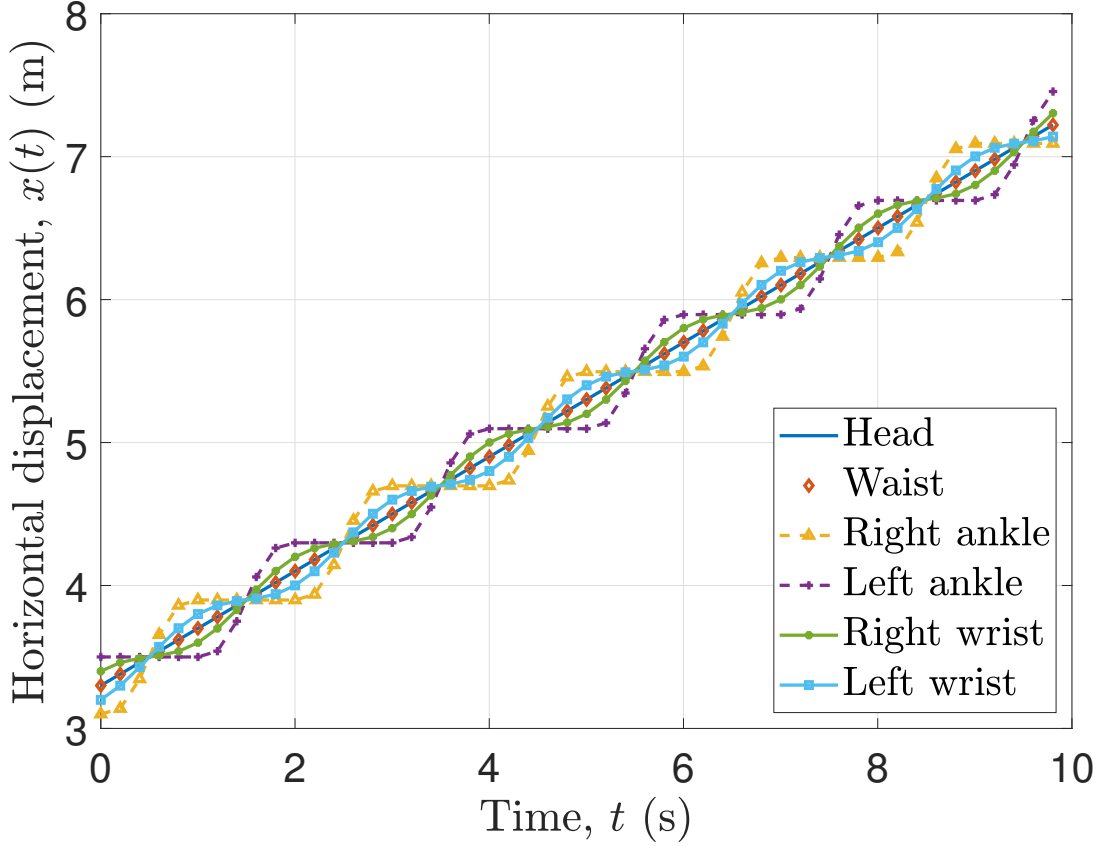
Figure C.2: TV forward displacements in the x-direction $x(t)$ of the 6-point scatterers representing the walking person.

AAOD $\alpha_{n,m,\mathrm{M}}^{T}(t)$, and EAOD $\beta_{n,m,\mathrm{M}}^{T}(t)$ from the displacement values and the values of the locations of the transmitter T_x and the receiver R_x. After that, the Doppler frequencies were computed using (C.1) and approximated using (C.3). Next, we integrated the Doppler frequencies of each moving scatterer w.r.t. time t. After that, each one of the integrated Doppler frequencies is added to an outcome of a random generator with a uniform distribution from $-\pi$ to π to obtain the instantaneous channel phase $\theta_{n,m,\mathrm{M}}(t)$ of each moving scatterer according to (C.5). For the fixed multipath components, which are not Doppler shifted, we obtained the associated phases $\theta_{m,\mathrm{F}}$ by generating the outcomes of a random generator with a uniform distribution from $-\pi$ to π for each scatterer. After performing the procedures described above, we obtained the complex channel gain $\mu(t)$ in (C.6). Fig. C.6 visualizes the approximated auto-term $S_{\mu}^{(a)}(f,t)$ of the spectrogram provided by (C.13). It can be shown that the resolution of the spectrogram improves after removing the cross-term by averaging the spectrogram $S_{\mu}(f,t)$ over the random channel phases $\theta_{n,m,\mathrm{M}}$ and $\theta_{m,\mathrm{F}}$. Fig. C.6 shows more clearly the influence of the fixed scatterers and the cluster of the moving scatterers on
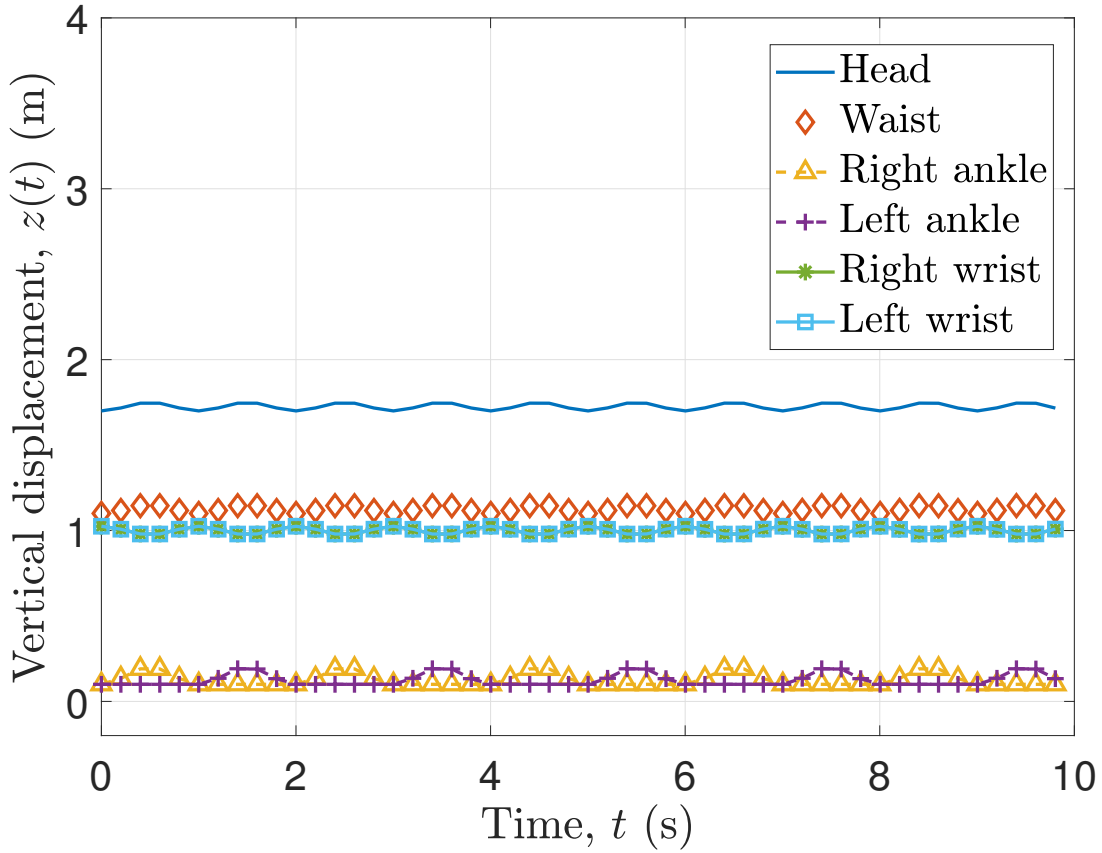
Figure C.3: TV vertical displacements $z(t)$ of the moving scatterers of the walking person.

the spectrogram. Note that the TV Doppler frequencies of the ankles in Fig. C.6 have the highest values that range from $-40\,\mathrm{Hz}$ to $40\,\mathrm{Hz}$.

Fig. C.7 depicts the TV mean Doppler shifts $B_f^{(1)}(t)$ and $B_\mu^{(1)}(t)$ computed according to (C.7) and (C.20), respectively. The spectrogram of $\mu(t)$ was simulated by using MATLAB. The TV mean Doppler shift $B_\mu^{(1)}(t)$ was computed numerically according to (C.20) using the approximate solution of the spectrogram $S_\mu(f,t)$ in (C.12), the simulated spectrogram, and the approximated auto-term $S_\mu^{(a)}(f,t)$ of the spectrogram in (C.13). It is shown in Fig. C.7 that the TV mean Doppler shifts obtained by using the spectrogram $S_\mu(f,t)$ are affected by the cross-term $S_\mu^{(c)}(f,t)$. There is a good match between the TV mean Doppler shift obtained by using the approximated solution of the spectrogram and the simulated spectrogram. Also, there is a good match between the TV mean Doppler shift $B_f^{(1)}(t)$ computed by (C.7) and the TV mean Doppler shift calculated by (C.20) using the auto-term $S_\mu^{(a)}(f,t)$.

Fig. C.8 depicts the TV Doppler spreads computed according to (C.8) and (C.21). The TV Doppler spread $B_\mu^{(2)}(t)$ was computed numerically according to (C.21) using the approximate solution of the spectrogram $S_\mu(f,t)$ in (C.12), the simulated spectrogram, and the approxi-
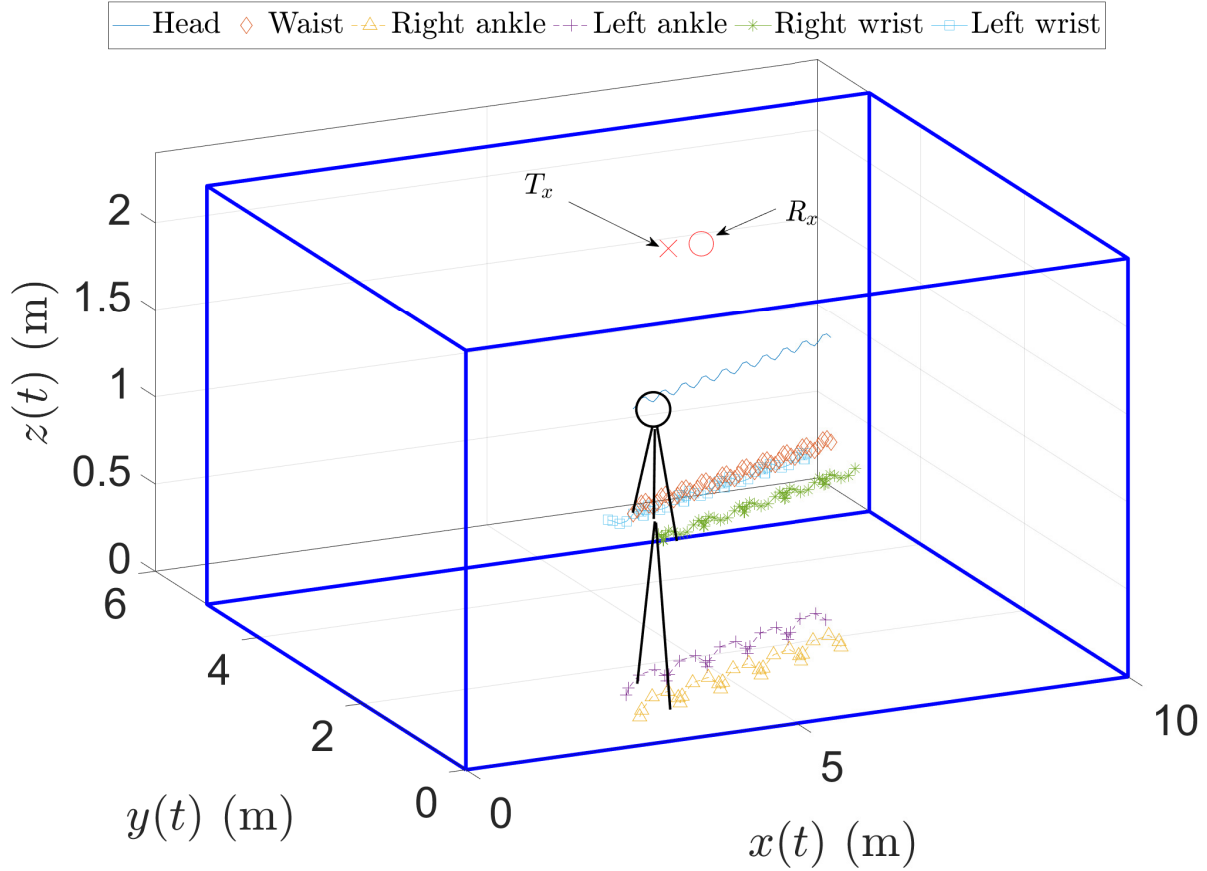
Figure C.4: Simulation scenario and 3D trajectories of the major body parts of a moving person.

mated auto-term $S_\mu^{(a)}(f,t)$ of the spectrogram in (C.13). It can be seen in Fig. C.8 that the TV Doppler spread $B_\mu^{(2)}(f,t)$ obtained by using the spectrogram $S_\mu(f,t)$ is affected by the cross-term $S_\mu^{(c)}(f,t)$. There is a good match between the TV Doppler spreads obtained by using the approximated solution of the spectrogram and the simulated spectrogram. The TV Doppler spread $B_f^{(2)}(f,t)$ computed by (C.8) and the TV Doppler spread $B_\mu^{(2)}(t)$ calculated by (C.21) using the auto-term $S_\mu^{(a)}(f,t)$ do not match. This is due to the influence of the variance $\sigma_{n,m,l,\mathrm{M}}^2$ and $\sigma_{m,\mathrm{F}}^2$ in (C.15) and (C.16) on the TV Doppler spread in (C.21), respectively, of the Gaussian functions of the auto-term $S_\mu^{(a)}(f,t)$.

C.6   Conclusion

In this paper, we introduced a 3D non-stationary channel model by modelling moving humans as clusters of synchronized moving scatterers to study the impact of major body parts of a walking person on the spectrogram of the complex channel gain of indoor F2F channels. We provided expressions for the TV Doppler frequencies and the TV phases of the
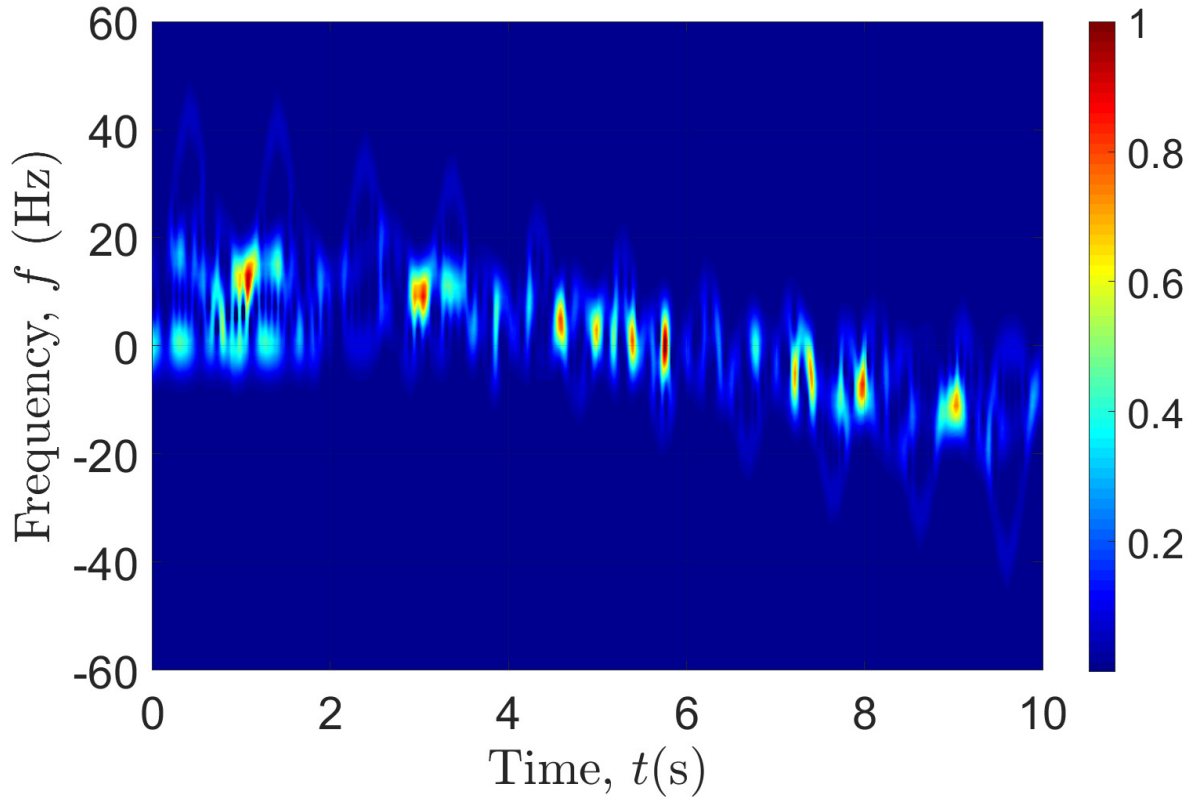
Figure C.5: Spectrogram $S_\mu(f, t)$ (analysis) of the complex channel gain $\mu(t)$.

moving scatterers representing the major body parts. Moreover, we presented mathematical expressions for the complex channel gain and showed the impact of a walking human on the spectrogram, for which an approximate solution has been presented. Furthermore, we presented trajectory models of different body parts of the walking human, such as ankles, wrists, head, and waist. Simulations validated the accuracy of the approximated-form of the spectrogram. For future work, we suggest validating the trajectory models and the channel model presented her in this paper with wearable IMU sensors and RF-measured data, respectively.
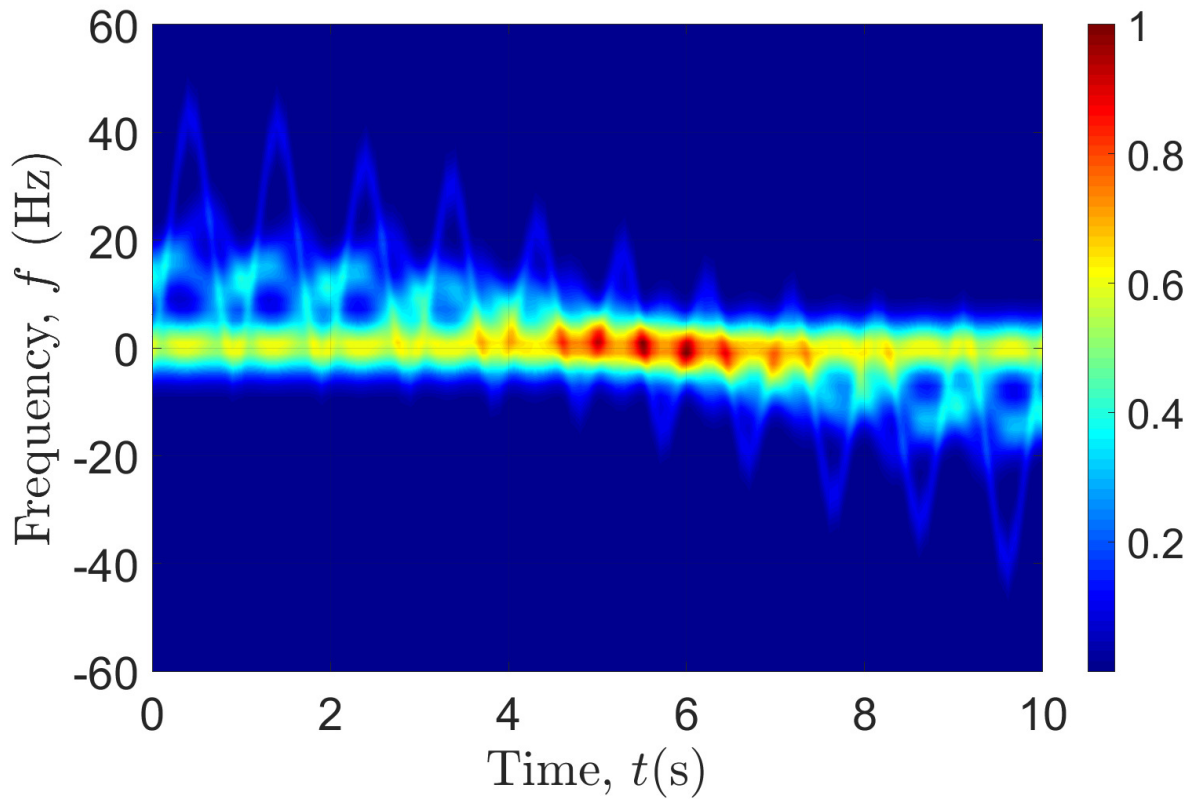
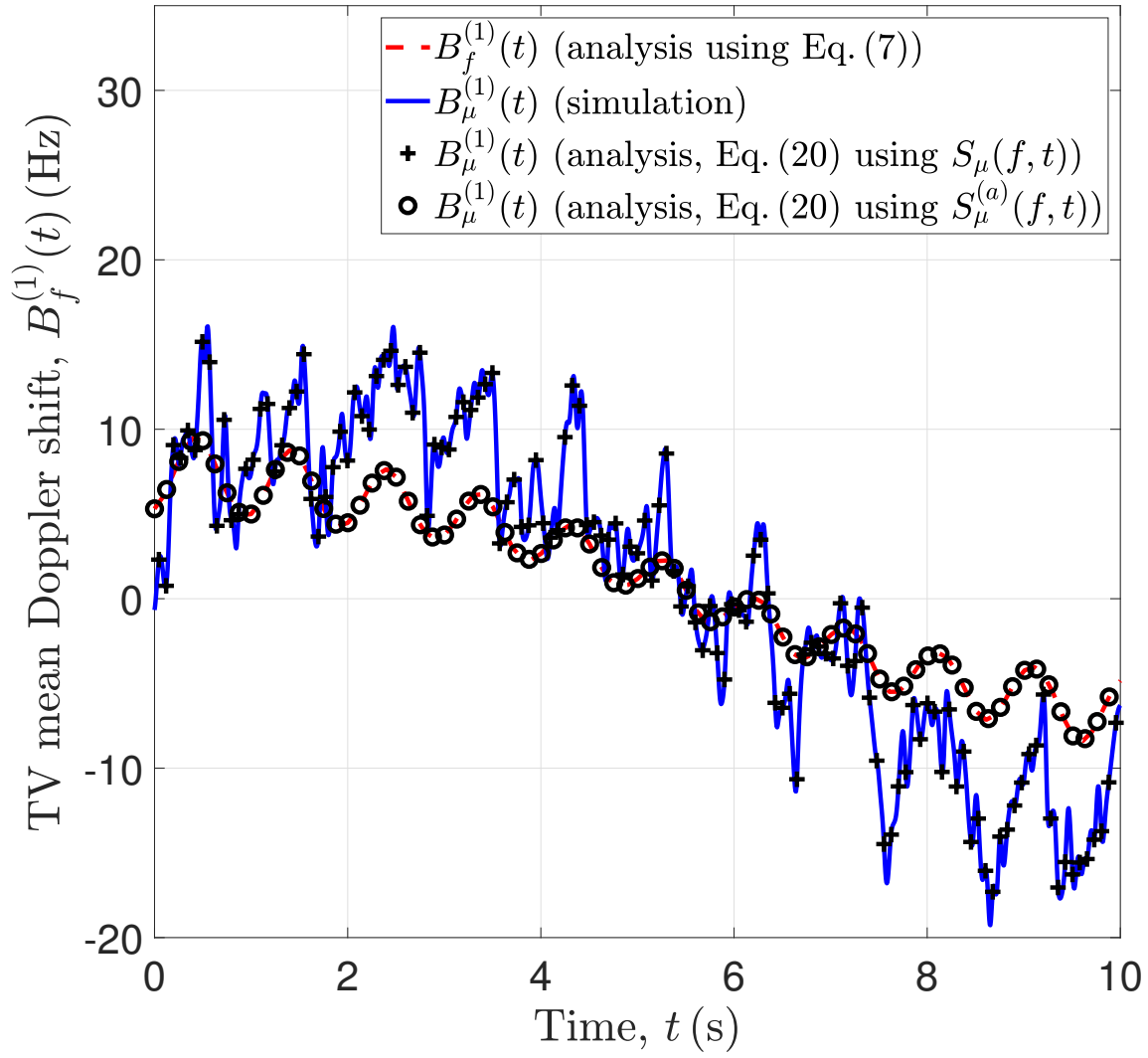Figure C.6: The auto-term of the spectrogram $S_\mu^{(a)}(f,t)$ (analysis) of the complex channel gain $\mu(t)$.

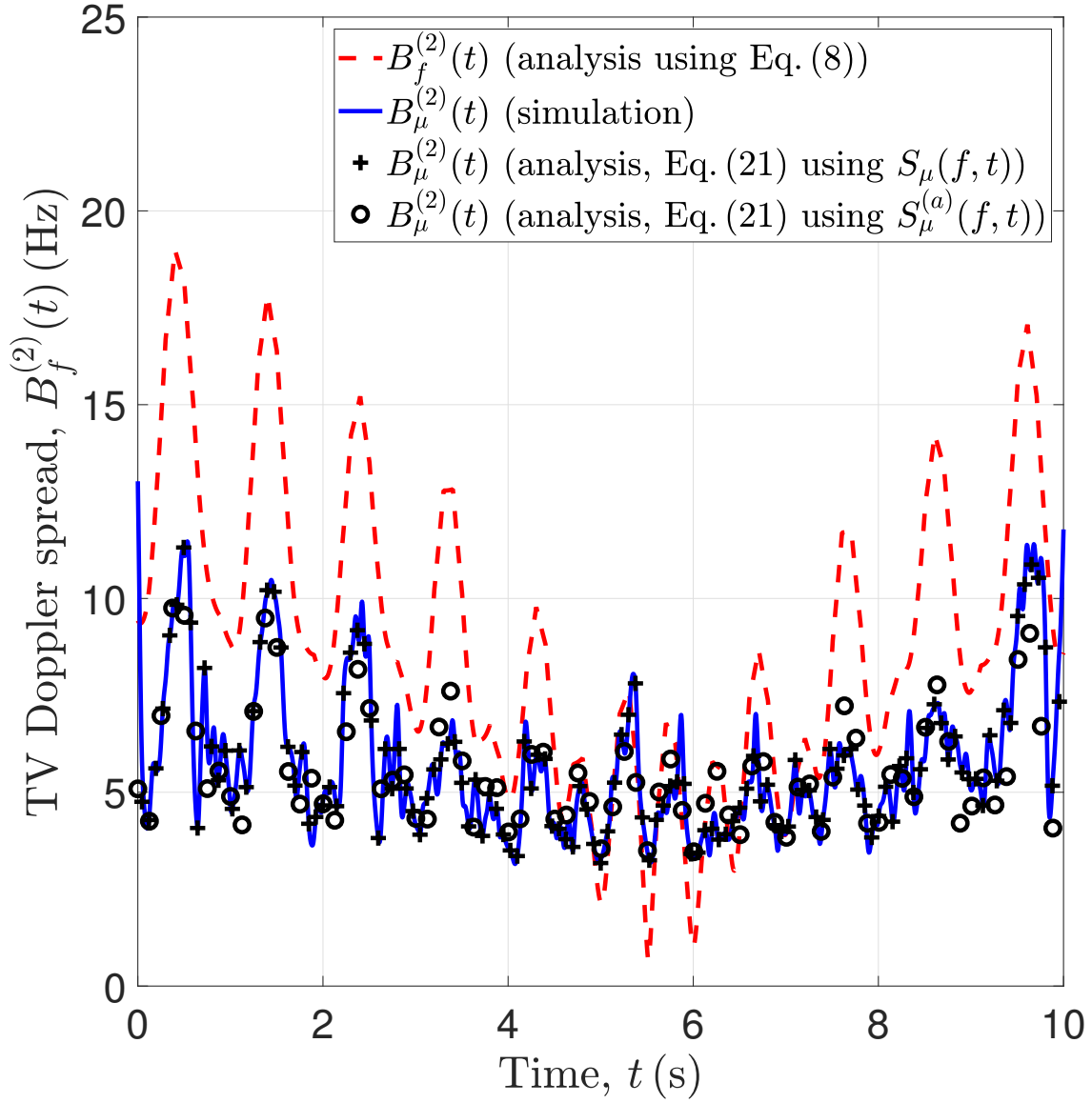Figure C.7: TV mean Doppler shift according to (C.7) and (C.20).

Figure C.8: TV Doppler spread according to (C.8) and (C.21).

Bibliography

[1] United Nations, Department of Economic and Social Affairs, Population Division , "World population ageing," 2017. Highlights (ST/ESA/SER.A/408).

[2] Y. Yan and Y. Ou, "Accurate fall detection by nine-axis IMU sensor," in *IEEE International Conference on Robotics and Biomimetics (ROBIO)*, pp. 854–859, Dec. 2017.

[3] V.-H. Pham, M.-H. Taieb, J.-Y. Chouinard, S. Roy, and H.-T. Huynh, "On the double Doppler effect generated by scatterer motion," *REV Journal on Electronics and Communications*, vol. 1, pp. 30–37, Mar. 2011.

[4] F. Adib, Z. Kabelac, D. Katabi, and R. C. Miller, "3D tracking via body radio reflections," in *Proc. of the 11th USENIX Conference on Networked Systems Design and Implementation NSDI'14*, (Berkeley, CA, USA), pp. 317–329, USENIX Association, 2014.

[5] A. Abdelgawwad and M. Pätzold, "On the influence of walking people on the Doppler spectral characteristics of indoor channels," in *Proc. 28th IEEE Int. Symp. on Personal, Indoor and Mobile Radio Communications, PIMRC 2017*, Montreal, Canada, Oct. 2017.

[6] A. Abdelgawwad and M. Pätzold, "A framework for activity monitoring and fall detection based on the characteristics of indoor channels," in *IEEE 87th Vehicular Technology Conference (VTC Spring)*, Porto, Portugal, Jun. 2018.

[7] J. Bian, C. Wang, M. Zhang, X. Ge, and X. Gao, "A 3-D non-stationary wideband MIMO channel model allowing for velocity variations of the mobile station," in *IEEE International Conference on Communications (ICC)*, pp. 1–6, May 2017.

[8] F. Hlawatsch and G. F. Boudreaux-Bartels, "Linear and quadratic time-frequency signal representations," *IEEE Signal Processing Magazine*, vol. 9, pp. 21–67, Apr. 1992.

[9] G. A. M, Y. D. Zhang, F. Ahmad, and K. C. D. Ho, "Radar signal processing for elderly fall detection: The future for in-home monitoring," *IEEE Signal Processing Magazine*, vol. 33, pp. 71–80, Mar. 2016.

[10] M. Wu, X. Dai, Y. D. Zhang, B. Davidson, M. G. Amin, and J. Zhang, "Fall detection based on sequential modeling of radar signal time-frequency features," in *IEEE International Conference on Healthcare Informatics*, pp. 169–174, Sep. 2013.

[11] Y. Kim and H. Ling, "Human activity classification based on micro-Doppler signatures using a support vector machine," *IEEE Transactions on Geoscience and Remote Sensing*, vol. 47, pp. 1328–1337, May 2009.

[12] F. Fioranelli, M. Ritchie, S.-Z. Gürbüz, and H. Griffiths, "Feature diversity for optimized human micro-Doppler classification using multistatic radar," *IEEE Transactions on Aerospace and Electronic Systems*, vol. 53, pp. 640–654, Apr. 2017.

[13] M. Pätzold and C. A. Gutiérrez, "Enhancing the resolution of the spectrogram of non-stationary channels by using massive MIMO techniques," in *Proc. IEEE 86th Vehicular Technology Conference, VTC2017-Fall*, Toronto, Canada, Sep. 2017.

[14] M. Pätzold, C. A. Gutiérrez, and N. Youssef, "On the consistency of non-stationary multipath fading channels with respect to the average Doppler shift and the Doppler spread," in *Proc. IEEE Wireless Communications and Networking Conference, WCNC 2017*, San Francisco, CA, USA, Mar. 2017.

[15] B. Boashash, *Time-Frequency Signal Analysis and Processing – A Comprehensive Reference*. Elsevier, Academic Press, 2nd ed., 2015.

[16] J. Liu and O. Urbann, "Walking pattern generation involving 3D waist motion for a biped humanoid robot," in *13th International Conference on Control Automation Robotics Vision (ICARCV)*, pp. 462–467, Singapore, Dec. 2014.

[17] J. Carpentier, M. Benallegue, and J.-P. Laumond, "On the centre of mass motion in human walking," *International Journal of Automation and Computing*, vol. 14, pp. 542–551, Oct. 2017.

[18] S.-U. Jung and M.-S. Nixon, "Estimation of 3D head region using gait motion for surveillance video," in *4th International Conference on Imaging for Crime Detection and Prevention 2011, ICDP 2011*, pp. 1–6, London, UK, Nov. 2011. DOI: 10.1049/ic.2011.0105.